

Small-Angle X-ray Scattering Using Coherent Undulator Radiation at the ESRF

D. L. Abernathy,^{a*} G. Grübel,^a S. Brauer,^b I. McNulty,^b G. B. Stephenson,^b S. G. J. Mochrie,^c A. R. Sandy,^c N. Mulders^d and M. Sutton^e

^aEuropean Synchrotron Radiation Facility, BP 220, 38043 Grenoble CEDEX, France, ^bArgonne National Laboratory, Argonne, IL 60439, USA, ^cMassachusetts Institute of Technology, Cambridge, MA 02139, USA, ^dUniversity of Delaware, Newark, DE 19716, USA, and ^eMcGill University, Montreal H3A 2T8, Canada. E-mail: aber@esrf.fr

(Received 12 September 1997; accepted 7 November 1997)

A simple approach for producing a high-coherent-flux X-ray beam for small-angle-scattering studies used at the Troika beamline of the European Synchrotron Radiation Facility is reported. For such small-angle studies it is permissible to reduce the longitudinal coherence length of the beam, thus increasing the energy bandpass and intensity of the beam, because there is only a small optical path-length difference. By using mirrors and filters to cut unwanted energies from the undulator harmonic structure, a high-flux beam of $>10^9$ photons s^{-1} through a 5 μm -diameter pinhole at 8.2 keV with a bandpass of 1.3% can be produced. The coherent properties of this beam have been measured by analyzing a static speckle pattern from an aerogel sample imaged by a directly illuminated CCD camera. The speckle size and contrast are compared with the expected values based on a statistical analysis of the intensity distribution of speckle patterns obtained using partially coherent conditions. The expected widths of the spatial autocorrelation are found, but there is an apparent incoherent fraction of the beam which reduces the measured contrast. The method presented is to be used as a tool to optimize conditions for diffraction experiments using coherent X-rays.

Keywords: coherent X-rays; speckle; intensity fluctuation spectroscopy.

1. Introduction

Undulator sources at third-generation synchrotrons provide an unprecedented *coherent* X-ray flux, enabling the exciting opportunity of measuring the low-frequency dynamics of disordered systems down to atomic length scales using intensity fluctuation spectroscopy techniques. The possibilities have been demonstrated by such pioneering studies as the observation of equilibrium critical fluctuations in the binary alloy Fe₃Al (Brauer *et al.*, 1995), dynamics of colloidal systems (Dierker *et al.*, 1995; Thurn-Albrecht *et al.*, 1996), and fluctuations in polymer micelle systems (Mochrie *et al.*, 1997). These techniques rely on the fact that when coherent light is scattered from a disordered system, it produces a highly modulated 'speckle' diffraction pattern that is uniquely related to the exact spatial arrangement of the illuminated material.

For systems not changing in time, this speckle pattern is static and can be used not only as an indication of the spatial structure of the sample but also as a tool for analyzing the coherence properties of the illuminating X-rays. In this paper we demonstrate the use of such a tool to characterize the properties of the high-coherent-flux beam produced by using simple mirror optics to isolate an undulator harmonic at the Troika (ID10A) beamline of the European Synchrotron Radiation Facility (ESRF) for small-angle scattering

experiments. Such a configuration allows the natural bandpass of the undulator to determine the longitudinal coherence length of the beam, which can be reduced for small-angle scattering because of the small optical path-length difference (Dierker *et al.*, 1995).

Fig. 1 shows the time-averaged small-angle scattering from an aerogel sample, collected using a charge-coupled device array (CCD) to measure the intensity by direct detection of the 8.2 keV photons (wavelength $\lambda = 1.63$ Å). The image covers a range in Q of ~ 0.03 Å⁻¹, where $\mathbf{Q} = \mathbf{k}_f - \mathbf{k}_i$ is the wavevector transfer of the scattering and $|\mathbf{k}_f| = |\mathbf{k}_i| = k = 2\pi/\lambda$. Good statistics for the intensity are ensured by averaging 200 1 s exposures of the CCD. A 5 μm -diameter pinhole was used to select a nominally coherent part of the X-ray beam. The graininess is the speckle pattern for the disordered gel, which in principle is directly related to the exact position of the scattering material in the illuminated volume as well as the coherence properties of the incident beam. Static speckle patterns using X-rays were first observed by Sutton *et al.* (1991) from antiphase domains in Cu₃Au, thereby demonstrating that properly collimating an incoherent source such as an X-ray insertion device gives coherent radiation. Other systems showing static speckle patterns include synthetic multilayers (Robinson *et al.*, 1995), Au-coated polymer films (Cai *et al.*, 1994), the charge-density wave system K_{0.3}MoO₄ (Pindak *et al.*, 1992)

and the binary alloy Fe_3Al (Brauer *et al.*, 1995; Bley *et al.*, 1995). The properties of small-angle speckle patterns from gels (Tsui *et al.*, 1998; Mainville *et al.*, 1997) and the alloy Al-Li (Mainville *et al.*, 1997) have also been measured.

There are many other methods of characterizing the coherent properties of synchrotron radiation. Diffraction from grating structures (Salditt *et al.*, 1994), imaging using phase contrast (Snigirev, 1996; Cloetens *et al.*, 1996), interference from Fresnel mirrors (Fezzaa *et al.*, 1997) and the time response of nuclear excitations in a moving ^{57}Fe foil (Baron *et al.*, 1996) have all been used recently to quantify the transverse coherence of X-ray radiation. The method presented here has the advantage for measurement and optimization of the coherence for X-ray intensity fluctuation spectroscopy (XIFS) that the sample can be mounted exactly as those to be used for dynamic studies, thus including effects of the sample environment. The detection system is the same as for XIFS, so that the entire chain of data collection is characterized. In addition, as we shall see from the statistical analysis, the longitudinal coherence and any incoherent part of the beam can also be analyzed.

Extracting meaningful information from a static speckle pattern about the exact arrangement of the sample is a daunting task (Robinson *et al.*, 1995), but by analyzing the intensity distribution for a speckle pattern one can learn about the properties of the radiation that produced it, including the illuminated volume size and degree of coherence. Properties of the beam, such as the monochromaticity, source size and nature of the optical elements in the path, all come into determining the statistical properties of

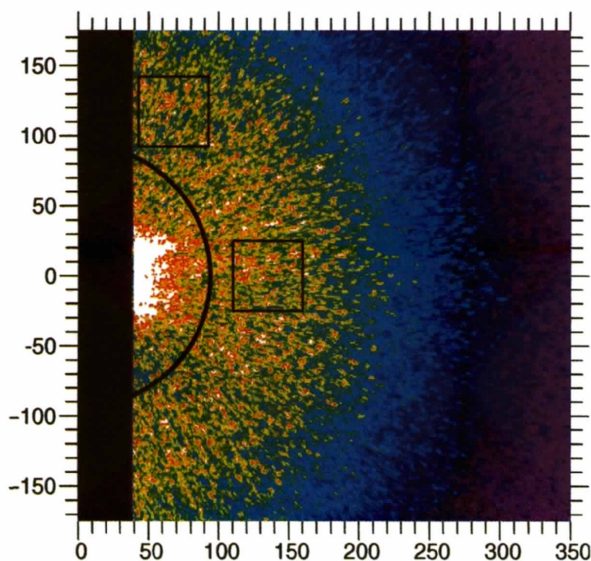


Figure 1

Speckle pattern from an aerogel using coherent X-rays produced by selecting an undulator harmonic with mirrors at the ESRF Troika beamline. Units are $22\ \mu\text{m}$ pixels relative to the direct beam location. The minimum Q used in the analysis, indicated by the black semicircle, was $0.007\ \text{\AA}^{-1}$. The image extends to $Q \simeq 0.03\ \text{\AA}^{-1}$.

the speckle intensities. In particular, the effects of the sample thickness on the speckle width and contrast are measured as well as the change in the statistics due to an incoherent part of the beam. We can use static speckle patterns to characterize the beam, thus allowing the optimization of the coherence for studies of dynamics.

2. Experimental methods

2.1. Beamline description

The experiments were performed at the Troika (ID10A) beamline of the ESRF, a multi-station beamline typically operating with transparent monochromators (Grübel *et al.*, 1994). The undulator source used in this study, located at a high- β straight section, is a standard ESRF 1.6 m-long 46 mm-period undulator with a 20 mm minimum gap. The storage ring of the ESRF currently operates with a horizontal emittance of 4 nm rad, calculated using root-mean-square (r.m.s.) values, and a vertical coupling of 1%, giving an electron beam full-width-at-half-maximum (FWHM) source size for the Troika beamline of $760\ \mu\text{m}$ (H) and $53\ \mu\text{m}$ (V), with FWHM divergences of $28\ \mu\text{rad}$ (H) and $4\ \mu\text{rad}$ (V). The beamline arrangement is given schematically in Fig. 2. Radiation from the undulator passes through a front end consisting of a 0.25 mm graphite filter and a 0.50 mm unpolished Be window at 23 m from the source. The primary slits of the beamline, located at 27 m from the source, were used to limit the X-rays to the central cone from the undulator and to control the effective source size. After a second unpolished 0.50 mm Be window and secondary slits, the beam was incident on a $50 \times 25 \times 7\ \text{mm}^3$ water-cooled Si mirror placed at the usual monochromator position 44 m from the source. After specular reflection, the beam passed through a 0.30 mm-thick diamond-film exit window. A lead beamstop in air after this window stopped the remaining unreflected beam, thus cutting the background in the experimental hutch to acceptable levels. After passing two evacuated flight paths with 0.08 mm Kapton windows, a nominally coherent part of the beam was selected by a $5\ \mu\text{m}$ -diameter pinhole aperture in an 80 μm -thick gold foil at a distance $R_s = 46\ \text{m}$

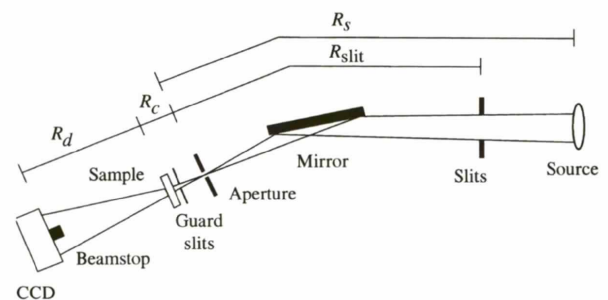


Figure 2

Schematic diagram of the beamline configuration showing major optical components and definitions of distances used in evaluating the static speckle pattern. Lines are guides to the eye indicating possible photon paths from the source to the detector.

from the source. The sample was at a distance $R_c = 100$ mm from the aperture, with a guard slit just in front of it to cut stray scattering from the windows and apertures. The sample scattering was measured using a CCD placed at a distance $R_d = 1.435$ m from the sample.

To check that the given beamline configuration is appropriate for producing a nominally coherent X-ray beam, we can estimate the coherence lengths using some simple approximations. The transverse coherence length, ξ_t , of the X-ray beam of wavelength λ for a source size d_s at a distance R_s is approximately given by

$$\xi_t = \lambda R_s / 2d_s, \quad (1)$$

and should be at least as large as the size of the aperture used to select the coherent portion of the beam. For 8.2 keV X-rays the transverse coherence lengths at 46 m from the source should be 4.5 μm horizontally and 65 μm vertically. The primary slits located at a distance $R_{\text{slit}} = 19$ m upstream from the aperture can also be used to set the effective size. For the image shown in Fig. 1 the horizontal primary slits were set to a width $d_{\text{slit}} = 0.25$ mm, giving a horizontal transverse coherence length of 5.7 μm . Thus, the 5 μm pinhole used should nominally be coherently illuminated.

The longitudinal coherence length, ξ_l , is determined by the monochromaticity of the beam and the wavelength,

$$\xi_l = \lambda^2 / 2\Delta\lambda, \quad (2)$$

and should be at least as large as the maximum optical path-length difference to be used in the experiment. In this work we are interested in small-angle scattering in transmission geometry, where these lengths are typically ~ 100 \AA . Thus, the bandpass can be relaxed to $\sim 1\%$, instead of the typical 10^{-4} for Si(111) monochromators, giving a much larger incident intensity. The advantages of this for diffraction using coherent X-rays have been demonstrated by Dierker *et al.* (1995), who used a multilayer monochromator at a wiggler source to perform XIFS of Au colloids.

The unusual geometry of replacing a monochromator or multilayer by a mirror was employed for this study to take advantage of the natural undulator source energy bandwidth. By varying the incidence angle of the mirror, different critical energies for the reflected beam could be chosen. Lower energies were eliminated by upstream carbon absorbers and beryllium windows. Energy spectra from the undulator after reflecting from the mirror are shown in Fig. 3. An Si(111) analyzer in horizontal scattering geometry and an NaI scintillation detector in integrating mode were used to measure the transmitted flux through 0.4 mm (H) \times 0.2 mm (V) slits *versus* energy. The detector acceptance was limited by slits in the diffraction plane to $\Delta(2\theta) = 1$ mrad, and scans were performed by moving the analyzer and detector angles in a 1:2 ratio ($\theta - 2\theta$ scans). The vertical scale was calibrated to give the number of photons per second for 160 mA ring current in the Si(111) bandpass and angular acceptance by measuring the scattering from a Kapton foil of known thickness using the scintillation counter (Grübel *et al.*, 1994). The measurements were

performed with the incidence angle of the mirror set to $\alpha_i = 0.175$ and 0.35° , corresponding to critical energies of 20 and 10 keV. Fig. 3 shows the third, fourth and fifth harmonics of the undulator with a gap of 21.7 mm, giving a fundamental harmonic of 3.05 keV.

The bandpass of the undulator was measured to be 1.3% FWHM for the third harmonic of the 35-period source. This value is consistent with the predicted bandpass

$$\Delta\lambda/\lambda = 1/nN, \quad (3)$$

where n is the harmonic number and N is the number of periods in the undulator. For the energy spectrum in Fig. 3 with the mirror set for a 10 keV cutoff, 85% of the counts shown are within twice the 1.3% FWHM bandpass around the third harmonic at 9.15 keV. For the measurements using the CCD, this harmonic rejection ratio should increase because of the decreased efficiency of the detector at higher energies compared with the scintillation counter. This method of using a simple mirror reflection should be well suited for small-angle scattering because of the limited optics involved and the improving methods of producing low-slope-error mirror surfaces for X-ray optics.

It is important to compare the measured flux with estimates based on calculations of the source flux and losses in the beamline optics. Using the *XOP* set of X-ray optics programs (Dejus & Sanchez del Rio, 1996), the peak flux through 0.4 mm (H) \times 0.2 mm (V) slits at 46 m is found to be 8.9×10^{12} photons s^{-1} (0.1% bandwidth) $^{-1}$ for the third harmonic at 9.1 keV and 160 mA ring current. This value must be corrected for the Si(111) bandpass ($1.3 \times 10^{-4}/0.1\% = 0.13$), horizontal primary slits ($R_s d_{\text{slit}}/R_{\text{slit}} d_s = 0.80$), mirror reflectivity (0.85), and absorption by air (0.90 m = 0.5), Be (1 mm = 0.87), carbon (0.55 mm = 0.64) and Kapton (0.56 mm = 0.85). The total estimated flux is thus 1.3×10^{11} counts s^{-1} , somewhat larger than the measured flux of 3.3×10^{10} counts s^{-1} .

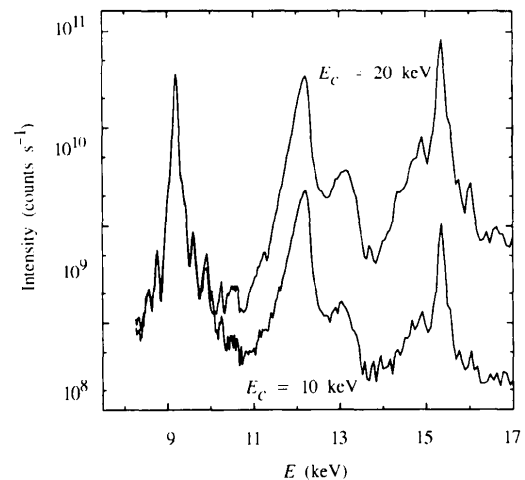


Figure 3

Energy spectra from the Troika undulator analyzed by an Si(111) reflection after a single mirror reflection. The nominal energy cutoff of the mirror was either 20 or 10 keV.

The flux through the 5 μm -diameter aperture was measured using the same Kapton scattering technique with the scintillation counter in differential mode after setting the undulator gap to produce 8.2 keV photons in the third harmonic and setting the mirror energy cutoff to just above this value. Typical rates were between $2\text{--}5 \times 10^9$ counts s^{-1} at 160 mA. The variation reflects the strong modulation of the vertical beam structure on lengths from 20–50 μm due to optical imperfections in the beamline elements, in particular the systematic surface variations of the unpolished Be window before the mirror. Integration of the flux in the third harmonic passing through an area equivalent to the circular pinhole at $R_s = 46$ m of a calculated spectrum for 160 mA gave 2.5×10^{10} photons s^{-1} . After correction for the primary slits (0.80), mirror reflectivity (0.85), and absorption by air (0.40 m = 0.64), Be (1 mm = 0.82), carbon (0.55 mm = 0.53) and Kapton (0.32 mm = 0.87), the expected flux is 4.1×10^9 counts s^{-1} . This value is consistent with using the calculated brightness of 6.0×10^{18} photons s^{-1} (0.1% bandwidth) $^{-1}$ mm^{-2} mrad^{-2} at 160 mA ring current. To within the accuracy of the calculation and the uncertainty of the flux measurement, the number of photons passing through the aperture is as expected.

It is interesting to note that while the analysis using the Si crystal found a factor of four loss compared with the calculated value, the measurement with a Kapton foil, which samples all of the radiation through the pinhole, found agreement with the theoretical value. The analyzer acts not only as an energy selector but also as a collimator, since it accepts only those X-rays within its Darwin width and which are within the detector acceptance. This fact was used, for example, by Cloetens *et al.* (1996) to determine the effects of random phase objects on the divergence of the beam, thereby measuring coherence losses. Apparently there is some extra divergence introduced by imperfections of the optics, which has little effect on the measurement just after the pinhole but appears as a loss of intensity for the analyzer configuration.

2.2. Sample and alignment

The sample used to produce the speckle patterns was a silica gel, made in a one-step process from a mixture of tetramethoxysilane, water and methanol catalyzed by NH_4OH . Silica gels exhibit a large range of correlations due to the diffusion-limited aggregation of the 10–20 \AA silica particles during gelation, and are of interest in many types of studies concerning the effects of random media and porous structures (Chan *et al.*, 1996). In this work the sample was 95% porous and 0.5 mm thick. Typical small-angle scattering from this sample, recorded using the CCD detector, are shown in Fig. 1. Strong scattering could be seen out to $0.03\text{--}0.04$ \AA^{-1} with a shoulder at ~ 0.01 \AA^{-1} , as seen in the circularly averaged scattering intensity shown in Fig. 4 as the open circles.

Also seen in Fig. 4 as the solid line is the scattered intensity along the horizontal direction for a single row of

pixels. There are deviations beyond counting statistics from the average scattering, which is the expected speckle structure seen when a disordered sample is coherently illuminated. The aerogel sample works well as a speckle producer because there is significant intensity over a large range of Q due to the fractal-like correlations in the sample. We note that the longest correlation length scale is of the order of 1000 \AA , so that it is possible to separate the contribution of the short-range correlations, which give the slowly varying Q -dependence of the average scattering, from the intensity variations due to the phase interference from different parts of sample that are uncorrelated, *i.e.* from the speckle structure. This allows an analysis of the speckle intensities to be made which is independent of the exact nature of the sample, as we show below.

Also seen in the scattered intensity, for the region where $Q \leq 0.007$ \AA^{-1} enclosed by the black arc in Fig. 1, is parasitic scattering from the direct beam. Besides having a beamstop for the beam passing directly through the sample to protect the CCD, seen as the dark box at the left of Fig. 1, it was found that a guard slit just at the sample was needed to cut parasitic scattering. This extra intensity, found to be in streaks coming from the beam center position, was attributed to excess scattering due to imperfections in the collimating pinhole. The use of the CCD camera, which could be viewed in real time to adjust the guard slit and beamstop to best cut this extra scattering, greatly facilitated the alignment.

2.3. Detector

The detector was a Princeton Instruments model CCD-576E thermoelectrically cooled CCD chip with 576×384 22 μm square pixels. It was designed for direct detection of X-rays, incorporating a thick depletion layer to achieve roughly 30% detective efficiency of the 8.2 keV photons. The camera was controlled by and the images stored on a Silicon Graphics workstation, using a custom-modified version of the program *Yorick* (Munro, 1995), which was

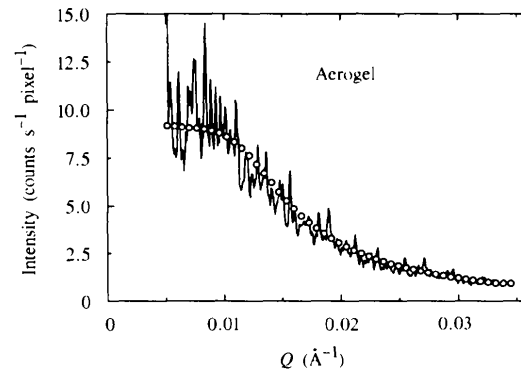


Figure 4

Circularly averaged scattering (circles) from the aerogel sample, normalized to give detected photons per second. The line is the intensity in one pixel row in the horizontal direction, showing the speckle structure. The intensity below $Q = 0.005$ \AA^{-1} is dominated by parasitic scattering of the pinhole and slits.

also used for image viewing and data processing. Data were acquired as a series of 1.00 s exposures, separated by 0.24 s for readout and storage of the images. Fig. 1 is the average of 200 such exposures, after subtracting an average dark image found from ten 1.00 s exposures with no X-ray beam on.

Owing to the limited dynamic range of the direct-detection CCD, the data must be taken as a time series. Using this sequence, it is possible to implement the statistical technique to characterize the CCD demonstrated by Dufresne *et al.* (1995). In brief, the idea of the method is that the mean and variance of the intensity measured in time at a given position of the scattering pattern should be related by Poisson counting statistics. For a perfect detector with no spreading of the signal between pixels and no electronic noise, the ratio of the variance over the mean will give the value in detector units of one photon. Spatial correlations and dark noise must be taken into account, as explained by Dufresne *et al.* (1995).

One change must be made for this procedure to be applied to speckle data. Since the signal itself is a strongly varying function on a length scale near the pixel size, the detector correlations or leakage between pixels must be found independently of any assumption about a uniform illumination of the detector. One possibility is to look at the individual exposures, where the statistics are dominated by photon counting and not the speckle intensity variations. By correlating individually these 1 s images and then averaging these correlations, a picture of the spreading of the signal is found. The solid symbols in Fig. 5 show that for this detector there is only significant leakage to the nearest neighbors, and it is symmetric in the two directions. This correction can be applied to the measured ratio of the time variance to the average intensity, giving a value of 240 ± 20 detector units per photon. This value was used to calibrate the intensity of detected photons shown in Fig. 4.

We note that an alternative approach is to analyze the individual clusters of charge, or ‘droplets’, resulting from the absorption of the X-rays. The total charge induced by single photon events can be seen directly, as well as the average spatial distribution. This technique can also distinguish multiple photon events. Applying such a droplet analysis to typical data taken with the detector gives a value of 238 ± 5 detector units per photon, as well as accounting for the correlations seen in Fig. 5 quantitatively (Livet, 1996).

3. Analysis of a static speckle pattern

In order to extract information about the coherence properties of the beam, we turn to a statistical analysis of the speckle pattern shown in Fig. 1. Speckle statistics have been well studied using laser light scattering, and the analysis of the effects of partial coherence, detector and source sizes and bandpass are known (Dainty, 1975; Goodman, 1985). In this section, this theory is applied to our X-ray speckle

pattern. In particular, it is important to consider the effect of the sample thickness, as well as losses of coherence due to the imperfections of the optical elements in the beamline.

To illustrate the technique, we calculate the statistical properties of the expected speckle pattern when the monochromatic incident radiation is perfectly coherent, and the detector resolution is much smaller than any spatial variation in intensity in the speckle pattern. It is convenient to calculate a normalized two-point intensity correlation function

$$C(\mathbf{r}_1, \mathbf{r}_2) = [\langle I(\mathbf{r}_1)I(\mathbf{r}_2) \rangle / \langle I(\mathbf{r}_1) \rangle \langle I(\mathbf{r}_2) \rangle] - 1. \quad (4)$$

The brackets $\langle \dots \rangle$ denote an ensemble average of an appropriate set of samples. Fig. 6 shows the coordinate system used to describe the experimental configuration. Points in the image are denoted by the vectors \mathbf{r}_i relative to the beam-zero position at the detector. Given a distance R_d from the sample to the detector and X-ray wavenumber $k = 2\pi/\lambda$, \mathbf{r}_i can be related to the wavevector transfer \mathbf{Q} , depending on the geometry. For the speckle pattern discussed in this paper, one can use the small-angle approximation that $|\mathbf{Q}| = k|\mathbf{r}|/R_d$.

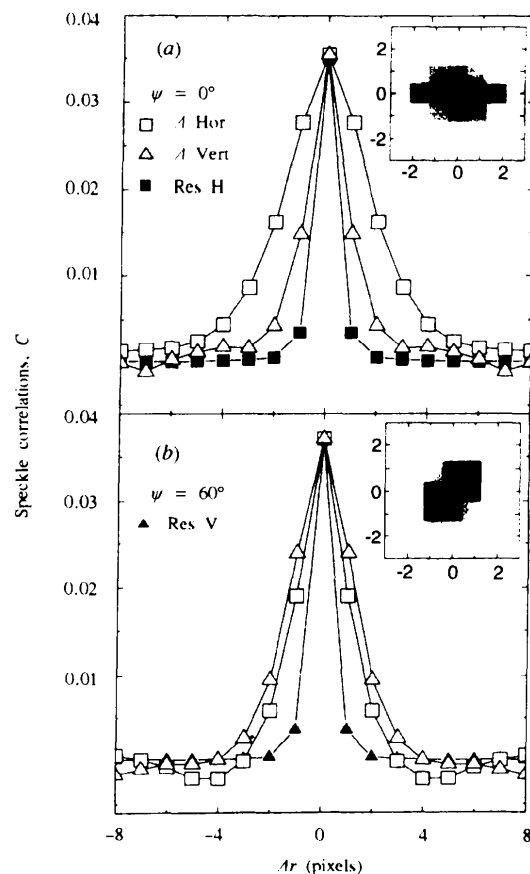


Figure 5 Insets: spatial autocorrelations for the areas outlined in Fig. 1 for azimuthal angle $\psi = 0^\circ$ (horizontal) (a) and $\psi = 60^\circ$ (b). Main figures: cuts in the horizontal (squares) and vertical (triangles) directions through the spatial correlations. Units are $22 \mu\text{m}$ pixels. The filled symbols represent the detector resolution found from averaged autocorrelations of the 1 s exposures.

We expect that the correlation function defined in (4) will peak at $\mathbf{r}_1 = \mathbf{r}_2$ and fall to zero for large separations. The FWHM of $C(\mathbf{r}_1, \mathbf{r}_2)$ is a reasonable measure of the size of the speckles. The contrast of the speckle pattern can be defined by the value

$$\beta(\mathbf{r}) = C(\mathbf{r}, \mathbf{r}). \quad (5)$$

In practice, instead of measuring many speckle patterns and then averaging over them, we assume the ensemble average is well approximated by taking an average over a suitable region of a single pattern. Then $C(\mathbf{r}, \mathbf{r} + \Delta\mathbf{r})$ is found from the normalized autocorrelation of an area centered at \mathbf{r} of a given detected speckle pattern.

To calculate the expected correlations explicitly, we write the intensity at a given point in the speckle pattern \mathbf{r} as the square of a total complex field $A_t[\mathbf{Q}(\mathbf{r})]$. We imagine that the sample can be divided into many small volumes $d\boldsymbol{\rho}$ such that each volume scatters with an amplitude $|A_0[\mathbf{Q}(\mathbf{r})]|$ given by the short-range correlations in the sample. However, these regions are assumed to be uncorrelated, so that the phase $\varphi(\boldsymbol{\rho})$ of this scattered field amplitude varies independently from region to region. This separation of length scales, such that any correlations in the sample are smaller than the illuminated volume, guarantees that the speckle statistics are characteristic of the incident radiation and detection scheme and not sample-dependent. The total field measured also depends on the incident radiation field $B(\boldsymbol{\rho})$ at each point in the illuminated volume and a phase term describing the change in phase due to the propagation of the field from the sample to the detector. Working in the far-field (Fraunhofer) regime, the intensity is then

$$I(\mathbf{r}) = |A_t[\mathbf{Q}(\mathbf{r})]|^2 = \left| \int B(\boldsymbol{\rho}) |A_0[\mathbf{Q}(\mathbf{r})]| \exp[i\varphi(\boldsymbol{\rho})] \exp[i\mathbf{Q}(\mathbf{r}) \cdot \boldsymbol{\rho}] d\boldsymbol{\rho} \right|^2. \quad (6)$$

The large variations in intensity as \mathbf{r} varies come from the interference of the different phase terms $\varphi(\boldsymbol{\rho})$ across the sample, thus giving the resulting speckle pattern its individual character. On average, correlations in the intensity for small $\Delta\mathbf{r}$ are given by the propagation of the scattering to the detector, thus giving a characteristic size to the speckles. Assuming that the incident intensity is

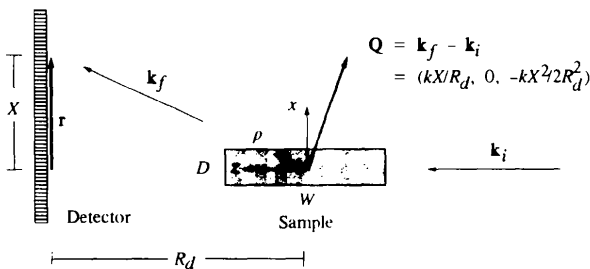


Figure 6
Schematic diagram of the scattering geometry and coordinates used to analyse static speckle statistics.

normalized, *i.e.*

$$\int |B(\boldsymbol{\rho})|^2 d\boldsymbol{\rho} = 1, \quad (7)$$

then the average intensity is simply

$$\langle I(\mathbf{r}) \rangle = |A_0[\mathbf{Q}(\mathbf{r})]|^2, \quad (8)$$

since in the average only the terms coming from the same point $\boldsymbol{\rho}$ survive.

The intensity correlation function defined in (4) is fourth order in the fields $A_t[\mathbf{Q}(\mathbf{r})]$. Because of the assumption that the fields are the sum of many independent phases, they obey circular complex Gaussian statistics (Dainty, 1975; Goodman, 1985). This may be thought of as a consequence of the central limit theorem, and the fields are considered as random walks in the complex plane. The result is that the fourth-order correlation function can be written as the sum of products of second-order correlations,

$$\begin{aligned} \langle I(\mathbf{r}_1)I(\mathbf{r}_2) \rangle &= \langle A_t[\mathbf{Q}(\mathbf{r}_1)]A_t^*[\mathbf{Q}(\mathbf{r}_1)]A_t[\mathbf{Q}(\mathbf{r}_2)]A_t^*[\mathbf{Q}(\mathbf{r}_2)] \rangle \\ &= \langle |A_t[\mathbf{Q}(\mathbf{r}_1)]|^2 \rangle \langle |A_t[\mathbf{Q}(\mathbf{r}_2)]|^2 \rangle \\ &\quad + |\langle A_t[\mathbf{Q}(\mathbf{r}_1)]A_t^*[\mathbf{Q}(\mathbf{r}_2)] \rangle|^2. \end{aligned} \quad (9)$$

Normalizing this result as defined in (4), we can write the intensity correlation function as

$$C(\mathbf{r}_1, \mathbf{r}_2) = |\mu_0(\mathbf{r}_1, \mathbf{r}_2)|^2, \quad (10)$$

with

$$\mu_0(\mathbf{r}_1, \mathbf{r}_2) = \int B(\boldsymbol{\rho})|^2 \exp \{ i[\mathbf{Q}(\mathbf{r}_1) - \mathbf{Q}(\mathbf{r}_2)] \cdot \boldsymbol{\rho} \} d\boldsymbol{\rho}. \quad (11)$$

We note that in the small-angle scattering approximation with monochromatic radiation, the function μ_0 , known as the complex coherence factor, depends only on the difference between the points $\Delta\mathbf{r} = \mathbf{r}_2 - \mathbf{r}_1$ and it has a contrast $\beta(\mathbf{r}) = 1$. In fact, for the case where the incident radiation $B(\boldsymbol{\rho})$ is constant within a given aperture and zero outside of that region, (10) and (11) show that the autocorrelation function of the speckle pattern follows exactly the form of the Fraunhofer diffraction pattern from the aperture (Goodman, 1975).

To see how the statistics of the measured speckle pattern compare with the ideal case, the normalized autocorrelation functions for two regions of Fig. 1 are shown in Fig. 5. Both areas, outlined by 50×50 pixel squares, are centered at the same $Q = 0.009 \text{ \AA}^{-1}$ but have different azimuthal positions ψ relative to the horizontal direction. It is found that a convenient way to calculate the autocorrelation is to first normalize the speckle pattern by the circularly averaged values corresponding to the radius of each pixel from the beam center. Then a fast Fourier transform technique can be used to calculate the autocorrelations (Dufresne *et al.*, 1995). By normalizing first, correlations due to the slow variations of the intensity are removed. Extra correlations at and near-zero displacement due to photon-counting statistics

must also be subtracted, using the measured resolution of the detector (Dufresne, 1995).

The insets in Fig. 5 show the normalized autocorrelations as two-dimensional gray-scale images, labeled by the displacements in pixels $\Delta \mathbf{r}$. In the main panels, cuts through the autocorrelation peak are shown for both the horizontal (open squares) and vertical (open triangles) directions. In Fig. 5(a) one can see that the correlations extend over a larger distance in the horizontal, which is the direction along \mathbf{Q} for the azimuth $\psi = 0^\circ$. In Fig. 5(b) this smearing is seen to rotate along with the direction of \mathbf{Q} . The elongation of the correlations along \mathbf{Q} is expected because of the broad bandpass of the radiation used (Dainty, 1975). The broadening also shows an interesting dependence, increasing from $\mathbf{Q} = 0$ until a maximum and then decreasing. To quantify this behavior, we must take into account the loss of resolution of the speckle pattern due to the variation in the wavenumber k , as well as the detector resolution and source sizes.

We can return to the calculation of the speckle statistics as outlined above, and include the possibility that there is a normalized distribution of wavenumbers $S(k)$ with a mean k_0 and that the detector has a normalized resolution given by $R(\mathbf{r})$, where \mathbf{r} varies over the surface of the detector. The equation for the detected intensity is then

$$I(\mathbf{r}) = \left| \int S(k) R(\mathbf{r} - \mathbf{r}') B(\boldsymbol{\rho}) |A_0[\mathbf{Q}(k, \mathbf{r}')] \times \exp[i\varphi(\boldsymbol{\rho})] \exp[i\mathbf{Q}(k, \mathbf{r}') \cdot \boldsymbol{\rho}] d\boldsymbol{\rho} dk d\mathbf{r}' \right|^2, \quad (12)$$

where we note explicitly that the momentum transfer \mathbf{Q} depends on both the wavenumber k and the position on the detector \mathbf{r} . Following the outline of the previous calculation, one arrives at a generalized version of the correlations in a partially coherent speckle pattern

$$C(\mathbf{r}_1, \mathbf{r}_2) = \int S(k') S(k'') R(\mathbf{r}_1 - \mathbf{r}') R(\mathbf{r}_2 - \mathbf{r}'') \times |\mu(k', k'', \mathbf{r}', \mathbf{r}'')|^2 dk' dk'' d\mathbf{r}' d\mathbf{r}'', \quad (13)$$

with

$$\mu(k, k', \mathbf{r}, \mathbf{r}') = \int |B(\boldsymbol{\rho})|^2 \exp \{i[\mathbf{Q}(k, \mathbf{r}) - \mathbf{Q}(k', \mathbf{r}') \cdot \boldsymbol{\rho}] \cdot \boldsymbol{\rho}\} d\boldsymbol{\rho}. \quad (14)$$

This is the complex coherence factor for partially coherent radiation, and the application of (13) and (14) to our conditions can be compared with the measured speckle statistics.

We first evaluate the effects of the integrations over the wavenumber spread $S(k)$. For illuminated sample volumes that are cylindrically symmetric about the incident beam, the dot product of \mathbf{Q} with $\boldsymbol{\rho}$ ensures that the transverse width of the correlations are unaffected by the wavenumber smearing (Parry, 1975). There is a broadening which is second order in the bandpass, as would be seen in the Fraunhofer diffraction from the aperture, which we neglect. Thus, we take the width derived from the monochromatic case, (10)

and (11), as the transverse width Δ_t . For the case of a circular pinhole with diameter D , the FWHM is

$$\Delta_t = 1.03(\lambda R_d / D d_p) \text{ (pixels)}$$

or

$$\Delta_t = 1.03(2\pi/D) \text{ (wavevector transfer)}, \quad (15)$$

in units of pixel size d_p and in reciprocal space units. For a slit of width W the formulae are the same with D replaced by W and the numerical factor replaced by 0.89.

In order to calculate the smearing of the correlations in the longitudinal direction Δ_l we must now apply (13) and (14). For convenience we work at zero azimuth and apply the small-angle approximation, as illustrated in Fig. 6. For $\mathbf{r} = (X, 0, 0)$ we have

$$\mathbf{Q}(\mathbf{r}) = (kX/R_d, 0, -kX^2/2R_d^2). \quad (16)$$

Taking $\boldsymbol{\rho} = (x, y, z)$, then the phase term in the complex coherence factor [equation (14)] is

$$\exp \{i[(kX - k'X')x/R_d - (kX^2 - k'X'^2)z/2R_d^2]\}. \quad (17)$$

If we assume that the incident intensity $|B(\boldsymbol{\rho})|^2$ is simply a constant within an illuminated volume defined by the pinhole of diameter D and the sample thickness W , then the integration over $\boldsymbol{\rho}$ in (14) yields

$$\mu(k, k', X, X') = \frac{\sin[(kX^2 - k'X'^2)W/4R_d^2]}{(kX^2 - k'X'^2)W/4R_d^2} \times \frac{2J_1[(kX - k'X')D/2R_d]}{(kX - k'X')D/2R_d}, \quad (18)$$

where J_1 is the Bessel function of the first kind. We take the wavenumber spread to be a Gaussian

$$S(k) = \exp[-(k - k_0)^2/2\delta^2 k_0^2], \quad (19)$$

with the width δ found from the FWHM bandpass of 1.3% by the relation for a Gaussian that the FWHM is $2[2(\ln 2)]^{1/2}\delta = 2.35\delta$. By numerically calculating the double convolution of (19) with (20) the wavenumber-smearing complex coherence factor μ_k can be found. This results in a peaked function of the position difference $\Delta X = X' - X$ with a maximum we denote β_k and an FWHM Δ_k .

The resolution of the system must also be taken into account before comparing the calculated speckle widths with experimentally found ones. If the resolution of the detector R is characterized by an FWHM Δ_R , then the double convolution in (13) leads to a reduction of the contrast approximately given by

$$\beta = \beta_k \Delta_k / (\Delta_k^2 + a\Delta_R^2)^{1/2}, \quad (20)$$

and a broadening

$$\Delta = (\Delta_k^2 + a\Delta_R^2)^{1/2}. \quad (21)$$

The parameter a depends on the shape of the resolution function, and is chosen to match the case where the width is dominated by the convolution of the resolution function

with itself. The results are exact if the resolution and complex coherence factor are Gaussian, using $a = 2$. Because the CCD detector has a box-like resolution of a single pixel d_p in width, as shown in Fig. 5, we use $a = 1$ since the convolution of a box with itself gives a triangle of FWHM equal to the box width.

There is also a loss in resolution due to the finite width of the incoherent source. Assuming that the same sample volume is illuminated, each point of the incoherent source contributes the same speckle pattern slightly shifted, since the pattern depends only on the product $\mathbf{Q}\cdot\rho$. Thus, after scaling by the ratio of the sample–detector and source–sample distances R_d/R_s , the source size can be taken into account in the same way as a detector resolution (McKechnie, 1975). Assuming the shape of the source is Gaussian with FWHM Δ_s , the corrections made to the contrast β_k and correlation widths Δ_k calculated from the wavenumber smearing due to the resolution are

$$\beta = \beta_k \Delta_k / (\Delta_k^2 + d_p^2 + 2\Delta_s^2 R_d^2 / R_s^2)^{1/2} \quad (22)$$

and

$$\Delta = (\Delta_k^2 + d_p^2 + 2\Delta_s^2 R_d^2 / R_s^2)^{1/2}. \quad (23)$$

The comparison of measured and calculated correlation widths is made in Fig. 7. Correlations in regions of Fig. 1 of 50×50 pixels in the horizontal direction centered at different Q values were evaluated, and the longitudinal FWHM Δ_l (open squares) and transverse FWHM Δ_t (open circles) for the spatial correlations C were found. In order to assess the error involved, the correlations at each Q were performed for azimuths varying in the range $-15 < \psi < 15^\circ$. The averages of Δ_l and Δ_t are plotted, with error bars given by the r.m.s. deviations. We note that at smaller Q the regions overlap significantly, so that the errors are under-

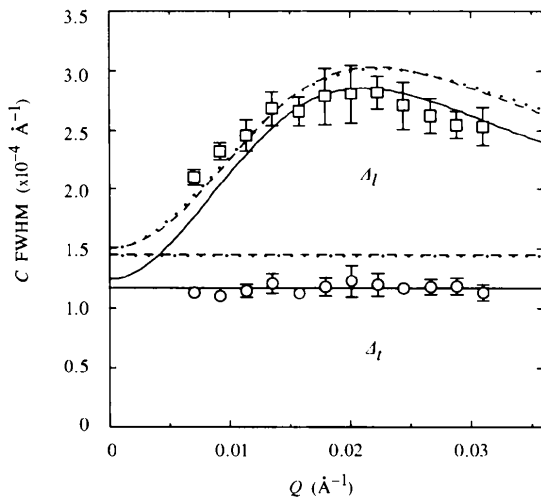


Figure 7

Correlation widths *versus* Q of the speckle pattern in Fig. 1 in the transverse (circles) and longitudinal (squares) directions. Lines are models of the widths based on evaluation of the complex coherence factor, as described in the text.

represented. The transverse widths are constant as a function of Q , as anticipated. At all Q the longitudinal widths are larger, as seen in Fig. 5, and for small Q Δ_l increases with Q as expected for the large bandpass. There is an unexpected crossover to decreasing longitudinal widths at higher Q . We take this to be the result of the loss of correlation due to the finite sample thickness, which at larger Q starts to dominate over the longitudinal smearing of the speckles.

The numerically calculated values of Δ_l and Δ_t using the pinhole diameter $D = 5 \mu\text{m}$, sample thickness 0.5 mm and r.m.s. bandpass $\delta = 0.013/2.35 = 0.0055$ are plotted as the dashed line in Fig. 7. Broadening due the detector resolution $\Delta_R = 1$ pixel and the scaled source sizes are included, as defined by (23). The difference in width at $Q = 0$ is due to the larger horizontal source size. The essential features of the widths are reproduced, including the decrease in Δ_l at larger Q . The values of the widths are, however, typically larger than measured.

For a better idea of how different parameters of the model affect the calculated widths, it is useful to make an approximate solution to the partially coherent correlations. Instead of the sharp illuminated volume, we can make a Gaussian approximation to the incident beam profile σ_D and to the thickness of the sample σ_W . Substituting

$$|B(\rho)|^2 = \frac{\exp(-z^2/2\sigma_W^2) \exp[-(x^2 + y^2)/2\sigma_D^2]}{(2\pi)^{3/2} \sigma_W \sigma_D^2} \quad (24)$$

into (14) gives the complex coherence factor for the Gaussian model

$$\mu_g(k, k', X, X') = \exp[-\sigma_D^2(kX - k'X')^2/R_d^2] \times \exp[-\sigma_W^2(kX^2 - k'X'^2)^2/4R_d^2]. \quad (25)$$

The convolutions with the Gaussian wavenumber spread in (13) can now be performed exactly. It is more useful to find the lowest-order terms in the bandpass $\delta \ll 1$ when the exact shape is compared with a Gaussian in the deviations $\Delta \mathbf{r}$ or $\Delta \mathbf{Q}$ by expanding about the peak at zero deviation. The result is that the transverse FWHM in this approximation Δ_t^g is given by

$$\Delta_t^g = 2(\ln 2)^{1/2} / \sigma_D \quad (26)$$

in reciprocal space units. The longitudinal FWHM Δ_l^g depends on Q , and is given by

$$\Delta_l^g = 2(\ln 2)^{1/2} \left(\frac{1 + 4\sigma_D^2 \delta^2 Q^2 + \sigma_W^2 \delta^2 Q^4 / k_0^2}{\sigma_D^2 + \sigma_W^2 Q^2 / k_0^2 + \sigma_D^2 \sigma_W^2 \delta^2 Q^4 / k_0^2} \right)^{1/2}. \quad (27)$$

The values of σ_D and σ_W can be set by requiring that the predicted widths should match those found for the calculation using the sharply defined illuminated volume. Numerically, this gives the values

$$\sigma_D = 2(\ln 2)^{1/2} D / 1.03(2\pi) = 0.26D, \quad (28)$$

and similarly

$$\sigma_W = 2(\ln 2)^{1/2} W / 0.89(2\pi) = 0.30W. \quad (29)$$

Using these values and convolving with the detector and source sizes as before, the dotted lines in Fig. 7 are calculated. The results are almost indistinguishable from the numerically calculated dashed lines, demonstrating that the approximations used are valid in the Q region studied.

It is interesting to examine (27) to see how the bandpass, pinhole size and sample thickness affect the longitudinal correlation widths. For a monochromatic beam ($\delta = 0$), the width decreases as Q increases. This is a result of the apparent increase in width of the sample for larger Q because of the sample thickness (Chu, 1974). If the sample has no thickness ($\sigma_W = 0$) then the width increases continuously for increasing Q . It is the interplay of the bandpass and sample thickness that causes the crossover from increasing to decreasing width *versus* Q . In fact, the peak of the width is determined in this approximation by

$$Q_{\max} = (k_0/\delta\sigma_W)^{1/2}, \quad (30)$$

giving $Q_{\max} = 0.0225 \text{ \AA}^{-1}$ for the parameters used to calculate the dotted line in Fig. 7.

Equations (26) and (30) allow the two size parameters σ_D and σ_W to be determined from the data directly. The measured transverse width, corrected for the detector and source sizes, is best fitted by taking $\sigma_D = 0.34D$, and $Q_{\max} = 0.02 \text{ \AA}^{-1}$ implies $\sigma_W = 0.34W$. Using these values gives the solid lines in Fig. 7, which accurately describe the data except for the small- Q longitudinal width. At small Q there may still be some stray scattering from the pinhole and guard slit which causes an excess width in the horizontal direction. The difference in σ_W is consistent with the accuracy to which the sample thickness is known. The increase in σ_D can be explained by the fact that the sample is not directly behind the pinhole, but the beam propagates a distance $R_c = 100 \text{ mm}$ and therefore can diverge before hitting the sample. The observed increase in size is a factor of 1.3, which seems reasonable given that R_c approaches the near-field cutoff of $D^2/\lambda = 165 \text{ mm}$.

Now that the correlation widths are reasonably well understood, we turn to the contrast of the speckle pattern, $\beta(Q)$. For the Gaussian model of the partial coherence, the predicted value from the wavenumber spread is found to be

$$\beta_k^g(Q) = (1 + 4\sigma_D^2\delta^2Q^2 + \sigma_W^2\delta^2Q^4/k_0^2)^{-1/2}. \quad (31)$$

This value is further reduced by the detector and source smearing according to (22) for both the longitudinal and transverse directions. This smearing introduces more Q -dependence because the longitudinal width also depends on Q . To see how this prediction compares with the measurement, the value for $Q = 0.0086 \text{ \AA}^{-1}$, using σ_D and σ_W determined from the widths, is calculated. The predicted total contrast is found to be $\beta = 0.38$, which is an order of magnitude larger than the measured value as seen in Fig. 5. Even though the speckle widths are well represented by a theory of partial coherence, which takes into account the effects of bandpass, detector and source sizes, we find that it does not predict the measured contrast.

To find a clue to help solve this discrepancy, we turn to another means of characterizing the statistics of a speckle pattern: the intensity probability distribution at a single point. For a speckle pattern where there are several independent coherence areas contributing, as in the case of partial coherence we have been developing, the intensity distribution is expected to follow approximately the gamma distribution (Dainty, 1975; Goodman, 1985)

$$p(I) = (M/\langle I \rangle)^M I^{M-1} \exp(-MI/\langle I \rangle)/\Gamma(M). \quad (32)$$

This distribution has a mean $\langle I \rangle$ and mean-squared deviation $\sigma_I^2 = \langle I \rangle^2/M$. The definition of contrast we are using is equivalent to $\beta = \sigma_I^2/\langle I \rangle^2 = 1/M$. For partially coherent speckle patterns the value of M is Q -dependent.

Fig. 8 shows the measured probability distribution for the intensities in an annulus where $0.0080 < Q < 0.0092 \text{ \AA}^{-1}$, plotted *versus* the intensity divided by the mean. Such distributions are easily calculated by histogramming the normalized speckle pattern used to determine the speckle widths. The gamma distribution [equation (32)] with mean and mean-squared deviations determined from the set of intensities ($M = 25$) is plotted as the dashed line. Apparently there are strong deviations from the expected distribution for partially coherent speckle patterns, even though the widths of the speckles are well predicted.

A closer examination of the measured intensity distribution shows that there are almost no scaled intensities below roughly 60–70% of the mean. This is common with other regions of the speckle pattern as well, indicating that there is a constant part of the incident beam which does not participate in the coherent interference leading to the speckle pattern. Calling the fraction of the beam which is described by the partial coherence theory α , one can show that the ‘incoherent’ fraction, $1 - \alpha$, reduces the measured

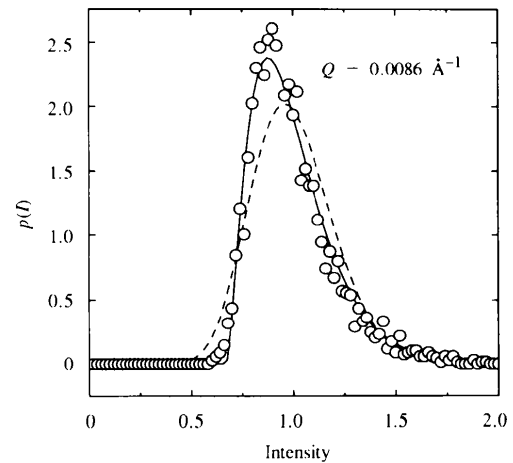


Figure 8

Intensity distribution of the 3432 pixels in an annulus where $0.0080 < Q < 0.0092 \text{ \AA}^{-1}$. The dashed line is the gamma distribution with the mean and variance of the measured distribution ($M = 25$), and the solid line is the gamma distribution after correcting for an incoherent background ($M = 2.7$).

contrast by a factor α^2 . It does not affect the widths of the speckle pattern, since it is a smooth function which follows the circularly averaged $\langle I(Q) \rangle$. The solid line in Fig. 8 is the gamma distribution that results if the mean and standard deviation are calculated after subtracting $1 - \alpha = 0.67$ from the scaled intensities ($M = 2.7$). There is better agreement with the measured intensity distribution.

As a final check of the consistency of the idea that only a fraction α of the beam contributes to the coherent scattering, the contrast as a function of Q can be compared with the calculated value scaled by α^2 . In Fig. 9 the circles are the measured contrast from the regions used to determine the speckle widths. Again, the errors are estimated from the azimuthal variations. The solid line is a calculation of the contrast in the Gaussian approximation [equation (31)] using values of σ_D and σ_W determined from the correlation widths, corrected for the detector and source sizes [equation (22)] in both directions and scaled by $\alpha^2 = 0.33^2$. This gives a reasonable match to the measured values, except at small Q where some slit scatter seems to affect both the width and the contrast.

4. Conclusions

At the Troika beamline of the European Synchrotron Radiation Facility, a high-coherent-flux X-ray beam for small-angle scattering studies has been produced. Using mirrors and filters to cut unwanted energies from the undulator harmonic structure provides $>10^9$ photons s^{-1} through a 5 μm -diameter pinhole at 8.2 keV with a bandpass of 1.3%. Such a beam makes studies of equilibrium dynamics at small wavevectors practical using the developing technique of X-ray intensity fluctuation spectroscopy, as has recently been demonstrated (Thurn-Albrecht *et al.*, 1996; Mochrie *et al.*, 1997).

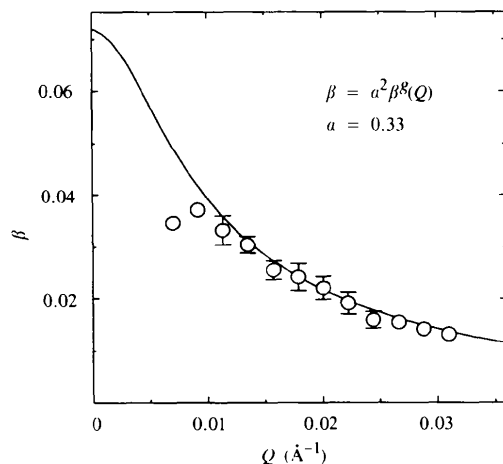


Figure 9

Contrast of the speckle pattern in Fig. 1 as a function of Q , calculated in the region used to measure the speckle widths. The solid line is calculated from a Gaussian model scaled by the square of the coherent fraction of the beam α .

Using a strongly scattering sample to produce speckle and an area detector, the coherence characteristics of a particular configuration can be measured in only a few minutes. This is a tool for evaluating and optimizing beamline optics and alignments for experiments using coherent radiation. At the same time, the procedure naturally leads to the characterization of the detector used.

A detailed analysis of the statistics of the static speckle pattern leads to the conclusion that the speckle widths can be described by the expected results from a partially coherent beam, taking into account the bandpass, detector and source sizes. In order to explain the intensity distribution and contrast, however, it must be assumed that only a fraction $\alpha \simeq 1/3$ of the beam scatters coherently. The rest of the beam acts as a background to reduce the contrast by α^2 . That the contrast is almost an order of magnitude below expected is also seen in XIFS experiments (Thurn-Albrecht *et al.*, 1996; Mochrie *et al.*, 1997), since the $\tau \rightarrow 0$ intercept of the time correlation function $g_2(\tau) - 1$ is also a measure of the contrast.

Possible sources of this 'incoherent' background are the random phase changes induced in the beam by non-ideal optical elements, such as the various windows and filters in the beam, as well as the mirror figure errors. Some part of the coherent beam is scattered out of the coherence volume on passing through each of these random phase objects. Thus, while the pinhole is meant to act as a spatial filter for coherence, there will be some of this scattered beam that passes through the pinhole and causes the reduction of the contrast. This conclusion is supported by the observation that the intensity of the beam is reduced from the expected value when measured using an analyzer, which acts as a collimator to reject the part of the beam scattered outside of its acceptance.

It is interesting to compare this study and its conclusions with another study of X-ray speckle statistics at the X25 wiggler beamline of the National Synchrotron Light Source by Tsui *et al.* (1998). That study, which used the same sample as the one employed here, concluded that the contrast was slightly reduced from the expected value and there was also less flux than expected. The present study finds a coherence which is a factor of nine too low, but the flux through the pinhole seems to be correct. The main difference in the measurements seems to be that the X25 configuration was more effective in reducing the loss of coherence, perhaps due to having fewer elements in the beam and to the fact that there was a larger distance between the pinhole and the main optical elements, which were a pair of multilayer monochromators.

Recent measurements at the Troika beamline after removal of several Kapton windows and polishing of the two beamline Be windows succeeded in increasing the contrast by a factor of three. It was observed that careful setting of guard slits all along the beamline was important in achieving the best contrast. We conclude that it is important to have optics which are as perfect as possible and to do the utmost to eliminate unwanted scattered radiation from

falling on the sample. Further experimental and theoretical studies are needed to better understand the origins of the observed coherence loss, in order to take full advantage of the newest synchrotron sources.

We wish to thank the staff of the Troika beamline for assistance with these experiments. Discussions with O. Tsui, E. Geissler, F. Livet and C. Sutter were much appreciated. Work at MIT was supported by the NSF (Grant DMR-9312543).

References

- Baron, A. Q. R., Chumakov, A. I., Grünsteudel, H. F., Grünsteudel, H., Niesen, L. & Rüffer, R. (1996). *Phys. Rev. Lett.* **77**, 4808–4811.
- Bley, F., Livet, F., Leroux, J. C., Simon, J. P., Abernathy, D., Als-Nielsen, J., Grübel, G., Vignaud, G., Dolino, G., Legrand, J. F., Camel, D., Menguy, N. & Papoular, M. (1995). *Acta Cryst.* **A51**, 746–750.
- Brauer, S., Stephenson, G. B., Sutton, M., Brüning, R., Dufresne, E., Mochrie, S. G. J., Grübel, G., Als-Nielsen, J. & Abernathy, D. L. (1995). *Phys. Rev. Lett.* **74**, 2010–2013.
- Cai, Z. H., Lai, B., Yun, W. B., McNulty, I., Huang, K. G. & Russel, T. P. (1994). *Phys. Rev. Lett.* **73**, 82–85.
- Chan, M., Mulders, N. & Reppy, J. (1996). *Phys. Today*, **49**(8), 30–37.
- Chu, B. (1974). *Laser Light Scattering*. Orlando: Academic Press.
- Cloetens, P., Barrett, R., Baruchel, J., Guigay, J.-P. & Schlenker, M. (1996). *J. Phys. D*, **29**, 133–145.
- Dainty, J. C. (1975). Editor. *Laser Speckle and Related Phenomena*. Berlin/Heidelberg/New York: Springer-Verlag.
- Dejus, R. J. & Sanchez del Rio, M. (1996). *Rev. Sci. Instrum.* **67**(9). (SR195; <http://www.esrf.fr/computing/expg/subgroups/theory/idl/xop/xop.html>.)
- Dierker, S. B., Pindak, R., Fleming, R. M., Robinson, I. K. & Berman, L. (1995). *Phys. Rev. Lett.* **75**, 449–452.
- Dufresne, E. (1995). PhD thesis, McGill University, Canada.
- Dufresne, E., Brüning, R., Sutton, M., Rodricks, B. & Stephenson, G. B. (1995). *Nucl. Instrum. Methods*, **A364**, 380–393.
- Fezzaa, K., Comin, F., Marchesini, S., Coisson, R. & Belakhovsky, M. (1997). *J. X-ray Sci. Technol.* **7**, 12–23.
- Goodman, J. W. (1975). *Laser Speckle and Related Phenomena*, edited by J. C. Dainty, p. 39. Berlin/Heidelberg/New York: Springer-Verlag.
- Goodman, J. W. (1985). *Statistical Optics*. New York: John Wiley & Sons.
- Grübel, G., Als-Nielsen, J. & Freund, A. K. (1994). *J. Phys IV*, **C9**, 27–34.
- Livet, F. (1996). Private communication.
- McKechnie, T. S. (1975). *Laser Speckle and Related Phenomena*, edited by J. C. Dainty, p. 143. Berlin/Heidelberg/New York: Springer-Verlag.
- Mainville, J., Bley, F., Livet, F., Geissler, E., Legrand, J. F., Abernathy, D., Grübel, G., Mochrie, S. G. J. & Sutton, M. (1997). *J. Appl. Cryst.* **30**, 828–832.
- Mochrie, S. G. J., Mayes, A. M., Sandy, A. R., Sutton, M., Brauer, S., Stephenson, G. B., Abernathy, D. L. & Grübel, G. (1997). *Phys. Rev. Lett.* **77**, 1275–1278.
- Munro, D. H. (1995). *Comput. Phys.* **9**, 609–615.
- Parry, G. (1975). *Laser Speckle and Related Phenomena*, edited by J. C. Dainty, p. 100. Berlin/Heidelberg/New York: Springer-Verlag.
- Pindak, R., Fleming, R. M., Robinson, I. K. & Dierker, S. B. (1992). Annual Report, BNL 52371, p. 381. National Synchrotron Light Source, BNL, Brookhaven, NY, USA.
- Robinson, I. K., Pindak, R., Fleming, R. M., Dierker, S. B., Ploog, K., Grübel, G., Abernathy, D. L. & Als-Nielsen, J. (1995). *Phys. Rev. B*, **52**, 9917–9924.
- Salditt, T., Rhan, H., Metzger, T. H., Peisl, J., Schuster, R. & Kotthaus, J. P. (1994). *Z. Phys. B*, **96**, 227–230.
- Snigirev, A. (1996). *SPIE J.* **2856**, 26–33.
- Sutton, M., Mochrie, S. G. J., Greytak, T., Nagler, S. E., Berman, L. E., Held, G. A. & Stephenson, G. B. (1991). *Nature (London)*, **352**, 608–610.
- Thurn-Albrecht, T., Steffen, W., Patkowski, A., Meier, G., Fischer, E. W., Grübel, G. & Abernathy, D. L. (1996). *Phys. Rev. Lett.* **76**, 5437–5440.
- Tsui, O. K. C., Mochrie, S. G. J. & Berman, L. E. (1998). *J. Synchrotron Rad.* **5**, 30–36.